Revised Version

CFD Analysis of High Frequency Miniature Pulse Tube Refrigerators for Space Applications with Thermal Non-Equilibrium Model

Abbreviated title: Modeling of Miniature Pulse Tube Cooler

Ashwin T.R[#], Narasimham G.S.V.L[#,$], Subhash Jacob[*]

[#] ***Department of Mechanical Engineering, Indian Institute of Science, Bangalore 560 012, India***
**** Centre for Cryogenic Technology, Indian Institute of Science, Bangalore 560 012, India***

Abstract

High frequency, miniature, pulse tube cryocoolers are extensively used in space applications because of their simplicity. Parametric studies of inertance type pulse tube cooler are performed with different length-to-diameter ratios of the pulse tube with the help of the FLUENT® package. The local thermal non-equilibrium of the gas and the matrix is taken into account for the modeling of porous zones, in addition to the wall thickness of the components. Dynamic characteristics and the actual mechanism of energy transfer in pulse are examined with the help of the pulse tube wall time constant. The heat interaction between pulse tube wall and the oscillating gas, leading to surface heat pumping, is quantified. The axial heat conduction is found to reduce the performance of the pulse tube refrigerator. The thermal non-equilibrium predicts a higher cold heat exchanger temperature compared to thermal equilibrium. The pressure drop through the porous medium has a strong non-linear effect due to the dominating influence of Forchheimer term over that of the linear Darcy term at high operating frequencies. The phase angle relationships among the pressure, temperature and the mass flow rate in the porous zones are also important in determining the performance of pulse tube refrigerator.

Keywords

Cryocoolers, Pulse tube, Regenerator, Oscillatory flow, Inertance Tube.

[$] Corresponding author. Tel: +91-80-2293 2971, Fax:+91-80-2360 0648
Email: mecgsvln@mecheng.iisc.ernet.in (Narasimham G.S.V.L)

Nomenclature

$A_{c,r}$ Total cross sectional area of regenerator (m^2)

A_p Porous cross sectional area regenerator (m^2)

A_s Total surface area (m^2)

A_t Total heat transfer area (m^2)

A_v Heat transfer area per unit volume (m^2m^{-3})

C Inertial resistance (m^{-1})

C_p Specific heat ($J\ kg^{-1}K^{-1}$)

D, d Diameter (m)

E Total energy ($J\ kg^{-1}$)

f Frequency (Hz)

h Heat transfer coefficient ($Wm^{-2}K^{-1}$)

k Thermal conductivity ($Wm^{-1}\ K^{-1}$)

L Length (m)

L_0 Amplitude (m)

L/D Length to diameter ratio.

M Mass (Kg)

n Wire mesh number

p Gauge pressure (Pa)

r_h Hydraulic radius of wire mesh (m)

S_Z, S_R Momentum source terms (Nm^{-3})

S_G, S_S Energy source terms (Wm^{-3})

T Temperature (K)

V Volume (m^3)

v Velocity (ms^{-1})

Greek symbols

τ Stress tensor (Pa)

ϕ Porosity

α Oscillating flow heat transfer coefficient between gas and solid matrix ($Wm^{-2}K^{-1}$)

β Permeability (m^2)

ρ Density (kgm^{-3})

μ Viscosity ($kg\ m^{-1}s^{-1}$)

ω Angular frequency ($rad\ s^{-1}$)

ψ Time constant

Subscripts

pt Pulse tube

reg Regenerator

f Fluid phase

s Solid matrix phase

r Radial direction

z Axial direction

1. Introduction

The Basic Pulse Tube Refrigerator (BPTR) was discovered by Gifford and Longsworth in the early 1960's [1]. The fundamental phenomena taking place in a BPTR were explained by de Boer [2]. Further modifications led to the development of Orifice Pulse Tube Refrigerator (OPTR) [3], Double Inlet Pulse Tube Refrigerator (DIPTR) [4] and multi-stage units. The OPTR and DIPTR achieved higher performance than the BPTR due to more favorable phase relationship between the oscillatory pressure and the mass flow rate. Another modification is the Inertance Pulse Tube Refrigerator (IPTR) in which an inertance tube (a long and narrow tube) replaces the orifice valve of OPTR (Fig.1a). The inertance tube imposes a hydraulic resistance and an inductance to the flow [5]. By varying the dimensions of the inertance tube, an adjustable delay between the pressure responses of the pulse tube and the reservoir can be created.

The compression and expansion process of gas inside the pulse tube is similar to that in a Brayton cycle. Gifford and Kyanka [1] explained the working of BPTR by the surface heat pumping (or bucket brigading) occurring due to the interaction of compressed gas with the walls of the pulse tube. This heat is conducted or pumped along the wall from cold heat exchanger to hot heat exchanger and finally rejected from the system. Rea [6] assumed that the convective heat transfer from oscillating gas to the walls of the pulse tube controlled the energy pumping. In the OPTR and other designs, the pressure heat pumping resulting from the proper phase angle between the pressure, temperature and mass flow rate is the major mechanism for energy transfer compared to the surface heat pumping [7].

For the most part, the models used for the analysis of pulse tube refrigerator are phasor type [5, 8], linear network type [9] and one-dimensional gas-dynamics type [10, 11]. It is only more recently that attempts have been made to use the full set of compressible equations with the help of fluid dynamics packages [12-14]. Some studies have also focused on the performance of regenerators under oscillating flow conditions [15]. There are also studies on the equivalent thermal conductivity of porous matrices such as sintered wire mesh screens [16, 17]. Such information is essential for the modeling of regenerators. Ashwin et al. [18, 19] made a comparative numerical study of inline and coaxial configurations of orifice and inertance type refrigerators using FLUENT, considering wall thickness and thermal non-equilibrium in porous zones.

The objective of the present work is the CFD analysis of a complete inertance pulse tube cooler with a minimum of simplifying assumptions. Parametric studies are conducted with different length-to-diameter ratios of the pulse tube. It should be noted that miniature coolers employ large L/D ratios for the pulse tube to obtain favorable cooling capacity [12]. The oscillating axi-symmetric flow and temperature fields in the various components of the IPTR are computed by solving the full set of compressible flow conservation equations. The porous zones are modeled taking into account the more realistic two-energy equation model, i.e. considering the thermal non-equilibrium between the gas and the matrix. Numerical studies have also been conducted for models with and without wall thickness. The wall thickness of individual components affects the dynamic characteristics especially at the time of cooldown. The effect of wall thickness is characterized in terms of a time constant of the pulse tube, which is the ratio of convective heat transfer to the heat stored in the walls. The effect of axial conduction on the performance of PTR is also taken into account. This numerical experimentation gives an idea about the mixing of gases inside the pulse tube zone, which indirectly affects the boundary-layer thickness and the heat transfer coefficient. These issues are addressed here for the first time with the help of CFD analysis.

2. PTR Geometry

Fig.1b shows the pulse tube model considered in this investigation along with the individual components. The wall materials for the various components are as indicated in Table 1.

3. Initial and Boundary Conditions

The swept volume of the compressor is 1.06 cm^3 and the clearance space is 0.17 cm^3. The initial charge pressure is 25 bar at an ambient temperature of 300 K. The working fluid is helium and is assumed to obey the ideal gas equation. The walls of the compressor after-cooler and hot heat exchangers are maintained at ambient temperature. Perfect cooling is

assumed in the compressor after-cooler. The cold heat exchanger wall is maintained at adiabatic condition (i.e., no load) as also the other walls of the system. The geometrical details and boundary conditions are listed in Tables 1 and 2. The wall thickness, wall material and the boundary conditions are common for all the models. The models differ in the L/D ratio of the pulse tube.

4. Modeling Details

The modeling of the geometry and nodalization of various parts are done using GAMBIT®. The junction regions of the components are represented with finer meshes for better numerical resolution. The number of grid points is varied from 4500 to 7200 in different models. Grid sensitivity studies are conducted for model 4 by keeping all other parameters constant. The number of nodal points to obtain consistent results is found to be 4500. Above 4500 grid points, there is no significant improvement in the precision of the numerical simulation. Dynamic meshing is used to model the compressor in which the volume of the domain changes with time. A User Defined Function (UDF) is written to track and properly guide the motion of the compressor piston with respect to time. The updating of the mesh is automatically done by FLUENT at each time step, depending upon the new position of the piston. Various dynamic meshing methods like "dynamic-layering", "remeshing" and "spring-based smoothening" are used for updating the meshing in the deforming volume. The operating frequency f is chosen as 50 Hz and the angular velocity is $\omega = 2\pi f$. The piston movement is traced by the relation $L = L_0 \sin(\omega t)$, where $L_0 = 3\times10^{-3}$ mm is the amplitude. The flow losses are determined by choosing appropriate values for inertial resistance, permeability and porosity. The porous zones are modeled by considering extra momentum sink terms in the momentum equations and the energy source or sink terms in the fluid and matrix energy equations.

5. Calculation of Other Parameters

The heat exchangers, namely, the compressor cooler, cold heat exchanger and the hot heat exchanger are taken to be porous media with a wire mesh number 325, permeability 1.06×10^{-10} m^2 and an inertial resistance of 76090 m^{-1} [11]. The matrix material is stainless steel for the regenerator and OFHC-Cu (Oxygen-Free High Conductivity Copper) for other heat exchangers. The porosity of wire mesh screens are given by $\phi = 1-\pi/(4x_t)$. The transverse pitch multiplier is given by $x_t = 1/(nd)$, where n is the mesh number and d is the wire diameter. The relations for the hydraulic radius r_h, porous cross-sectional area A_p and the

transfer area A_t are $r_h = d[(x_t/\pi) - (1/4)]$, $A_p = \phi A_{c,r}$ and $A_t = LA_p/r_h$ .The equivalent diameter is $D_e = 4r_h$.

The viscosity, thermal conductivity and specific heat of the working gas and the solid matrixes are taken to be temperature dependent. The temperature dependent thermo-physical properties are obtained from the NIST database. User Defined Functions (UDFs) for the calculation of variable thermophysical properties of the working medium and the porous matrixes are written and appropriately hooked to the FLUENT panel [20].

6. Governing Equations

The governing equations, namely, the continuity, momentum and energy equations are written for a cylindrical coordinate system with the assumption of axi-symmetry and no swirl. The velocity components appearing in the equations are the superficial velocity components in the case of porous zones [18].

6.1 Continuity Equation

$$\frac{\partial}{\partial t}(\rho_f) + \frac{1}{r}\frac{\partial}{\partial r}(r\rho_f v_r) + \frac{\partial}{\partial z}(r\rho_f v_z) = 0 \qquad \text{----------(1)}$$

6.2 Momentum Equation in Axial Direction

$$\frac{\partial}{\partial t}(\rho_f v_z) + \frac{1}{r}\frac{\partial}{\partial z}(r\rho_f v_z v_z) + \frac{1}{r}\frac{\partial}{\partial r}(r\rho_f v_r v_z) = -\frac{\partial p}{\partial z} + \frac{1}{r}\frac{\partial}{\partial z}\left[r\mu\left(2\frac{\partial v_z}{\partial z} - \frac{2}{3}\left(\vec{\nabla}\bullet\vec{v}\right)\right)\right] + \frac{1}{r}\frac{\partial}{\partial r}\left[r\mu\left(\frac{\partial v_z}{\partial r} + \frac{\partial v_r}{\partial z}\right)\right] + S_Z \qquad \text{----------(2)}$$

6.3 Momentum Equation in Radial Direction

$$\frac{\partial}{\partial t}(\rho_f v_r) + \frac{1}{r}\frac{\partial}{\partial z}(r\rho_f v_z v_r) + \frac{1}{r}\frac{\partial}{\partial r}(r\rho_f v_r v_r) = -\frac{\partial p}{\partial r} + \frac{1}{r}\frac{\partial}{\partial z}\left[r\mu\left(\frac{\partial v_z}{\partial r} + \frac{\partial v_r}{\partial z}\right)\right] + \frac{1}{r}\frac{\partial}{\partial r}\left[r\mu\left(2\frac{\partial v_r}{\partial r} - \frac{2}{3}\left(\vec{\nabla}\bullet\vec{v}\right)\right)\right] - 2\mu\frac{v_r}{r^2} + \frac{2}{3}\frac{\mu}{r}\left(\vec{\nabla}\bullet\vec{v}\right) + S_R \qquad \text{----------(3)}$$

The source terms S_Z and S_R are zero for non-porous zones. Separate axial and radial momentum source terms are included in the porous zones to account for the momentum losses. The resistance of the flow through the porous media is accounted by two terms, namely, the Darcy term in which the pressure drop is directly proportional to velocity and a Forchheimer term, in which the pressure drop is proportional to the square of the velocity. The solid matrix is assumed to be homogeneous. The momentum source terms in the porous zones in the axial and radial directions are respectively

$$S_Z = -\left(\frac{\mu}{\beta} v_z + \frac{1}{2} C \rho_f |v| v_z\right) \text{ and } S_R = -\left(\frac{\mu}{\beta} v_r + \frac{1}{2} C \rho_f |v| v_r\right). \text{ ----------(4, 5)}$$

6.4 Energy Equations for the gas and the matrix

In describing the temperature distribution in a porous zone, the thermal equilibrium assumption is often invoked for simplifying the formulation. Under this assumption, the energy equation reads:

$$\frac{\partial}{\partial t}\left(\phi \rho_f E_f + (1-\phi)\rho_s E_s\right) + \vec{\nabla} \bullet \left(\vec{v}\left(\rho_f E_f + p\right)\right) = \vec{\nabla} \bullet \left(k \vec{\nabla} T_f + \left(\tau \bullet \vec{v}\right)\right) \text{ ---------- (6)}$$

$$k = \phi k_f + (1-\phi) k_s \text{ ---------- (7)}$$

where $E_f = \hat{h} - p/\rho_f + v^2/2$ ---------- (8)

In the thermal equilibrium model, the temperatures of the gas and solid structure are the same at any time and spatial location. Thus, in this model, the thermal interaction between the fluid and the matrix is neglected by describing the temperature distribution with a single energy equation for the gas and matrix put together. The thermal non-equilibrium model accounts for the heat interaction between the solid and gas. This requires the solid matrix and the interstitial fluid to be described by separate energy equations. The heat transfer coefficient between solid and fluid can be calculated using standard correlations. This model accounts for the thermal losses in the porous zones. In components like regenerators, where thermal inertia plays an important role, the non-thermal equilibrium consideration tends to be more accurate. The energy equations for the matrix and the gas in thermal non-equilibrium model are as follows:

6.5 Energy Equation for Matrix

$$\frac{\partial}{\partial t}\left(\rho_s E_s\right) = \vec{\nabla} \bullet \left(k_s \vec{\nabla} T_s\right) + S_S \text{ ---------- (9)}$$

$$\text{i.e: } \frac{\partial}{\partial t}(\rho_s C p_{,s} T_s) = \frac{1}{r}\frac{\partial}{\partial r}\left[k_s r \frac{\partial T_s}{\partial r}\right] + \frac{\partial}{\partial z}\left[k_s \frac{\partial T_s}{\partial z}\right] + \frac{\alpha A_v (T_f - T_s)}{1-\phi} \text{ ---------- (10)}$$

6.6 Energy Equation for Gas

$$\frac{\partial}{\partial t}(\rho_f E_f) + \vec{\nabla} \bullet \left(\vec{v}\left(\rho_f E_f + p\right)\right) = \vec{\nabla} \bullet \left(k \vec{\nabla} T_f + \left(\tau \bullet \vec{v}\right)\right) + S_G \text{ ---------- (11)}$$

For non-porous zones, the energy source term S_G is zero. However, in the porous zones $S_G = \alpha A_v \left(T_s - T_f\right)/\phi$.

6.7 Heat transfer coefficient between porous structure and the working gas

For pulsating flow, heat transfer coefficient in the regenerator is given by Tanaka et al. [15]:

$$\alpha = 0.33 \frac{k_{\mathrm{f}}}{D_{\mathrm{e}}} \left(\frac{\rho_{\mathrm{f}} D_{\mathrm{e}}}{\mu} \frac{2 V_{\mathrm{p}} \rho^{*}}{A_{\mathrm{s}} \phi} \right)^{0.67} \quad \text{---------- (12)}$$

where $\rho^{*} = \rho_{\mathrm{f}}(T_{\mathrm{H}}) / \rho_{\mathrm{f}}(T_{\mathrm{av}})$. The quantities T_{av} and T_{H} are respectively the average temperature of the gas inside the regenerator and the hot end regenerator temperature.

6.8 Effective thermal conductivity of porous structure

From Koh and Fortini [16], the thermal conductivity of solid matrix can be obtained by neglecting the contribution of the helium gas. The resulting relation is:

$$K_s = \frac{1-\phi}{1+11\phi} K \quad \text{---------- (13)}$$

6.9 The Time Constant

The time constant for pulse tube wall or porous zones is defined as the ratio of heat stored in the pulse tube wall (or porous matrix) to the convective heat transferred to the pulse tube wall (or porous matrix). The dynamic characteristics of the different pulse tube models can be evaluated by introducing a time constant for the pulse tube as well as porous zones. Here ψ represents the time constant, M the mass of the system, h the heat transfer coefficient between wall (or matrix) and the gas and A_s, the total surface area. In case of regenerator A_s can be calculated from the expression:

$$A_s = \frac{6(1-\phi)V_{reg}}{d_h} \quad \text{---------- (14)}$$

where V_{reg} is the total volume of the regenerator and d_h is the wire diameter used in the regenerator mesh.

$$\psi = \frac{MC}{hA_s} \quad \text{---------- (15)}$$

6.10 The compressor input power

$$\dot{W} = \frac{1}{\tau} \oint p_{\mathrm{v,a}} \frac{dV}{dt} dt \quad \text{----------(16)}$$

where $p_{\mathrm{v,a}}$ is the volume-averaged pressure in the swept volume of the compressor.

7. Method of Solution

7.1 Algorithm

Unsteady pressure based segregated solver with implicit formulation is used for solving the discretized equations. First order method is used for unsteady terms as a compulsory option because of the dynamic meshing. The algorithm used is SIMPLE with suitable under-relaxation parameters to attain the convergence. FLUENT can solve the additional equation in a domain or zone with the help of certain functions called User-Defined Scalars (UDSs). The solution of the additional equations in the porous zone is accomplished with the help of separate UDSs. The general scalar transport equation defined with the help of the UDSs contains four terms, namely, the unsteady term, convection term, diffusion term and the source term. These terms are properly customized and attached to the UDSs with the help of User defined Functions (UDFs). The second order upwinding is used for convective terms. The absolute convergence criterion is 0.001 for the continuity, radial and axial velocities, and for the User Defined Scalars, while it is 10^{-6} for temperature. Preliminary numerical experimentation revealed that with the initial condition at room temperature (300 K), typically 500 seconds of real time is needed to reach an oscillatory state with a time step of 0.0005 seconds. At each time step, 50 inner iterations are used for proper coupling between the equations and for better convergence. It is observed that over 25 days of CPU is required for the system to reach a periodic state on a SUN work station with 3 GHz processor and 2 GB of RAM. The terms VAMS (Volume Average Mean Static), FAMST (Facet Average Mean Static), FA (Facet Average), VA (Volume Average) are defined in [20]. The term Mean refers to the average over one cycle.

7.2 Validation with previously published works

In order to determine the accuracy of the algorithm and the method of solution, a validation study is conducted against the previously published work of Cha et al. [12] with thermal equilibrium of regenerator and without considering the wall thickness of each component. Fig.2 shows that the present cooldown curve is almost identical with that of Cha et al. Moreover, the no-load steady-state temperature of 85.3 K reached with the present model using 3525 grid points, a times step of 3 ms and 20 inner iterations per time step compares favourably with the value of 87 K reported by Cha et al. using 4200 nodal points.

8. Results and Discussion

8.1 Temperature and pressure distributions during cooldown and steady state

Fig.3a shows the Facet Average (FA) pressure and temperature variation at the exit of cold heat exchanger for the first 120 time steps (i.e. at the starting period) of the pulse tube geometry that considers the wall thickness and thermal non-equilibrium of porous zones (Model 4). The oscillatory temperature profile at the exit of cold heat exchanger still shows a

downward trend at this time while the pressure profile almost attains a periodic state. This shows a rapid change in temperature compared to pressure. Fig.3b shows the cyclic variation of temperature and pressure for the same model at 432.2685 seconds, after reaching a periodic state. The temperature at the exit of the cold heat exchanger oscillates between 116 K and 124 K and the pressure oscillates between 17 bar and 23 bar over one cycle. The pressure in the system attains a mean value of 21 bar from the charging pressure of 25 bar, after reaching the periodic condition.

Form Figures 3a and 3b, it can be noted that the variation of temperature or pressure over one cycle is not exactly sinusoidal. This is due to the complex interaction of the solid matrix and the gas in the cold heat exchanger. The high thermal mass of porous zones and the pulse tube wall promote heat storage. The thermal damping effects of porous zones and the pulse tube wall as well as temperature-dependent properties of the solid and the fluid could also be responsible for this kind of distorted temperature and pressure profiles. The figures clearly show the phase lag between the mass flow rate and pressure at the exit of cold heat exchanger. Similar conclusion can be drawn with respect to the distortion occurring in the pressure profiles. The distortion in the temperature profile also affects the pressure profile due to the coupling. The physical property variation of the working gas will influence the Darcy and Forchheimer terms; in turn it affects the pressure drop through porous zones. There is a marginal distortion in temperature profile while the distortion in pressure profile is very insignificant.

Fig.4a shows the regenerator pressure variation with thermal non-equilibrium of the porous zones. The momentum losses in the porous zones are accounted for by Equations 4 and 5. As mentioned, the two terms contributing to momentum losses are the Darcy and Forchheimer terms. At the instant under consideration (432.668 seconds), it can be seen that a pressure drop of about 1 bar is occurring in the regenerator.

Fig.4b shows the axial temperature variation in the system. It may be recalled that perfect cooling is assumed in the compressor after cooler. It can be seen that a good temperature gradient is established axially between the regenerator, pulse tube and the hot heat exchanger respectively. The modeling is done with thermal non-equilibrium model of the regenerator. The figure also shows the axial temperature gradient maintained in the regenerator. High thermal mass (combined with lower thermal conductivity of regenerator matrix) is favorable for establishing good axial temperature gradient; it may be noted that the high thermal mass tends to lengthen the cooldown. However, due to finite conductivity, there will be a small thermal or exergy loss in the regenerator. The heat pumping through the pulse tube can be

clearly seen. It can also be seen that the temperature decreases from the entry to exit of the cold and hot heat exchangers. The temperature variations in the inertance tube and the buffer are not significant compared to other regions.

Fig.4c shows the velocity vector plots. It can be seen that two-dimensional effects are more prominent at the junctions between the components. This emphasizes the need for a multidimensional model rather than one dimensional model, which fails to capture the actual flow distribution effects. Due to the connection of the transfer line (a small diameter tube) and the compressor cooler in this geometry, the flow will be mainly confined to the central parts of the compressor cooler and regenerator. It will be advantageous to distribute the flow from the transfer line over the entire cross-section of the compressor cooler and regenerator. This is likely to result in a more rapid cooldown.

8.2 Cool down Characteristics with Different L/D ratios

Fig.5a shows the Volume Average Mean Static Temperature (VAMST) of the cold heat exchanger plotted against the cooldown time for different pulse tube models, with the average taken over one cycle. These results are obtained for models with finitely thick walls with thermal equilibrium assumption for the porous zones. The influence of pulse tube length on the performance of various models is evaluated based on the cooldown temperature in the cold heat exchanger.

The Fig.5b shows the variation of compressor input power versus the L/D ratio of different pulse tube models. The work done by the compressor can be calculated using Equation 16. Nearly linear increase in compressor input power can be noticed with increase in the L/D ratio of the pulse tube due to higher viscous losses in the system. This is due to the fact that longer pulse tube needs higher pumping power.

From Fig.5a, the pulse tubes with smaller L/D ratio are seen to stabilize at a higher cold heat exchanger temperature while the minimum temperature reached by models decreases as the L/D ratio increases. The lowest cold heat exchanger temperature is attained at an optimum L/D ratio for Model 5. It is expected that accounting for wall thickness of the pulse tube leads to more realistic modeling of the cooldown process. The mechanism of cooling can be explained as follows:

The three fluid zones that can be identified in the pulse tube cooler are the cold gas zone near the cold heat exchanger, pulse tube gas in the central zone and the hot gas zone near the hot heat exchanger. The pulse tube gas in the central zone acts as a buffer between the other two zones, preventing the mixing of the cold and hot gas zones. Pulse tubes with smaller length to

diameter ratio tend to even out the temperature gradient across the pulse tube because of the mixing of gases from the three zones as well as axial heat conduction. This prevents the cold heat exchanger from attaining the lowest possible temperature. For very large L/D ratio, the volume of pulse tube central gas zone exceeds the optimum volume required to prevent mixing of cold and hot gas zones. This gas volume does not involve in active heat transfer processes and can result in higher frictional dissipation leading to increased compressor work and decreased overall effectiveness or the coefficient of performance. At the same time, the amount of axial heat conduction decreases with increase in L/D ratio which improves the performance as shown in Fig.5a. Both compressor work and the cooling capacity should be considered before selecting a particular pulse tube design.

8.3 Effect of Finite Wall thickness

The Facet Average Mean Static Temperature (FAMS) of the working gas at the exit of cold heat exchanger for Model 3 is plotted against the cooldown time in Fig. 6. The modeling of porous zones is done with thermal equilibrium. The FLUENT gives the flexibility of modeling a pulse tube system with and without solid wall. The pulse tube model without wall takes only 200 seconds to reach 95% of the steady state temperature of 65 K while the model with wall takes almost 450 seconds to reach the steady state temperature of 130 K. From this it is evident that the effect of wall thickness will increase the temperature attained in the cold heat exchanger. The model with finitely thick wall of 0.3 mm represents the actual cool down taking place in pulse tube since it captures the significant contribution of axial conduction and also the small amount of surface heat pumping process. The wall thickness of the pulse tube and the regenerator affects the time-lag between the cooldown process and the thermal stabilization time. The wall thickness increases the thermal mass and thus the thermal storage of the whole system. During cooldown, the gas core of the cold heat exchanger attains a lower temperature at a faster rate compared to the outer wall. Gradually the wall also attains a lower temperature due to thermal penetration. The decrease in temperature near cold heat exchanger establishes an axial temperature gradient along the wall of the pulse tube and the regenerator. The effect of axial heat conduction from hot heat exchanger side and the regenerator side are mainly responsible for the higher cold heat exchanger temperature and larger cooldown time of a given pulse tube model. Subsequently the thermal gradient becomes larger as the cooldown progresses. The heat transfer due to this axial conduction is not instantaneously transferred to the gas. Consequently the system takes longer time for stabilization. This is can be also explained by introducing pulse tube and porous zone time constants.

Fig.7a shows the variation of Volume-Average Mean Static Temperature (VAMS) and area averaged surface heat transfer coefficient between pulse tube wall and the gas versus time constant of pulse tube wall after reaching a periodic state. The heat transfer coefficient is the average value over one cycle. The observations are also presented in Table 3. The convective heat transfer in the pulse tube appears to be one of the major mechanisms affecting the pulse tube performance, as also reported in [6], among other sources. It is observed that the heat transfer coefficient is higher for smaller length pulse tubes because of the turbulent mixing of gases inside the pulse tube. The resulting turbulence will influence the thermal boundary-layer thickness and the convective heat transfer between pulse tube wall and the gas. The time constant has an inverse relation with the convective heat transfer coefficient as well as the convective heat transfer area. Higher heat transfer coefficients facilitate pumping of more heat to the pulse tube wall during cooldown process. Therefore the cold end temperature decreases with increase in time constant of pulse tube wall, i.e., the pulse tube configuration with smaller L/D ratio settles at a higher cold heat exchanger temperature. In reality the effect of time constant of pulse tube wall and the mixing of the gases in the three zones also play a major role in the process of heat pumping. It is also required to keep a minimum length in the pulse tube region to avoid mixing of gases between cold heat exchanger zone, central gas zone and hot heat exchanger zone, as already mentioned. The longer pulse tube may produce lower temperature but it is inefficient due to higher viscous dissipation.

Fig.7b shows the variation of area averaged temperatures of the pulse tube wall and the fluid, and the heat transfer coefficient. This can give an idea of the temperature variation in the pulse tube solid and fluid portions over one cycle. It can be observed that the temperature decrease of pulse tube wall temperature is slow compared to the fluid temperature which changes rapidly over one cycle. At some instances of the cycle the gas temperature is above the solid temperature. The heat pumping from gas to solid takes place during this half cycle. At other instances, the gas temperature is below the solid temperature and the heat is pumped from solid to the gas. The duration shown is for two cycles after a time of 1.0435 seconds has elapsed after startup from the ambient (300 K). These results are expected since the heat capacity of solid is larger compared to that of the working gas. More heat will be pumped from solid to gas during initial stages of cooldown. The cooldown of solid will be slower compared to the working gas. The heat pumped from solid to gas will be finally rejected at the hot heat exchanger.

Fig.7c shows the amount of axial conduction from cold heat exchanger side and the heat transfer between pulse tube gas and solid during one cycle (with reference to Fig.7b). Heat

transfer to gas from pulse tube wall is taken as positive. The quantities calculated are the averages over the surface area over time step. Average solid temperature at pulse tube inlet and outlet are used to calculate axial conduction according to Fourier's law. It can be clearly observed that the axial conduction is steadily increasing as the system cools down because the temperature difference across the pulse tube increases. Fig.7c also shows that the amount of pulse tube gas-solid heat transfer (surface heat pumping) is more compared to the axial conduction. This reveals that surface heat pumping can also be one of the major mechanisms in the cooldown of high frequency pulse tube systems.

Table 3 shows the dynamic response of the pulse tube configuration with wall and with thermal equilibrium assumption in the regenerator. The cooldown time (t_{90}) is defined as the time needed to reach 90% of the cold heat exchanger temperature. It can be seen that the time constant, which combines the heat transfer coefficient and the thermal mass of the pulse tube wall, directly affects the cooldown characteristics of the whole system. Increase in the thermal mass of the pulse tube wall increases the cooldown time (Table 3) because the pulse tube wall acts as a thermal flywheel. The cooldown time in seconds follows a relation $t_{90} = 385.32\psi_{\text{pt}} + 3.679$ where t_{90} is the cooldown time and ψ_{pt} is the time constant of pulse tube wall. The time constants of the regenerator and other porous zones are very small compared to the time constant of pulse tube wall as shown in Table 4. Thus the time constants of the porous zones have negligible effect on the dynamic characteristics of the system.

8.5 The Effect of Local non-thermal equilibrium in Porous Zones

Thermal non-equilibrium takes into account the heat transfer between gas and matrix, while thermal equilibrium does not distinguish between the matrix and gas temperatures. This means in the latter model, the heat transfer coefficient tends to infinity. A comparison of the results with these two models is presented in Fig.8a, where the Facet Average Mean Static (FAMS) Temperature is plotted against the cooling time. The analysis presented here is with wall thickness for Model 4. A case with thermal non-equilibrium of porous zones and finite wall thickness represents a realistic model. The thermal equilibrium model exhibits rapid cooling followed by leveling off of the temperatures, while the thermal non-equilibrium model shows comparatively gradual cooling and stabilization of temperatures. The thermal non-equilibrium model takes longer time (above 400 seconds) for reaching the steady state while the thermal equilibrium model attains steady state much earlier, i.e., in about 200 seconds. The final temperature reached with thermal equilibrium model is lower than that of the thermal non-equilibrium model. This is due to the fact that the thermal non-equilibrium

model implicitly takes into account the thermal losses in the regenerator. The thermal losses occurring in the porous zones are mainly responsible for the decrease in performance. However, from the point of view of heat transfer, the accuracy of the heat transfer correlations can have an effect on the validity of the results obtained for the thermal non-equilibrium case. Figures 8b and 8c shows the temperature profile after 440 seconds for the solid matrix and the gas inside regenerator and hot heat exchanger for Model 4 with wall thickness. The thermal non-equilibrium between the gas and the matrix is of the order of 0.01 K after reaching a steady periodic condition. The non-thermal equilibrium model is more realistic for the cooldown process.

Figures 9a and 9b shows the variation of Darcy term and Forchheimer term with velocity over two periods after reaching steady periodic condition for Model 4 with wall thickness. It may be recalled that modeling of porous zones also requires pressure drop correlations in addition to the heat transfer correlations. The pressure drop correlations are influenced by the properties of the fluids which are functions of temperature. Thus the heat transfer correlations also indirectly affect the pressure drop through the porous medium. As mentioned earlier, the two terms contributing to the pressure drop in the porous medium are the Darcy and Forchheimer terms. In the Darcy term $\mu v/\beta$, the pressure drop is proportional to the velocity and in Forchheimer term $\left(C\rho_f |v|v\right)/2$, the pressure drop is proportional to the square of the velocity. From Figures 9a and 9b it can be seen that the non-linearity due to Forchheimer term is prominent at high frequencies since its contribution to the pressure drop is significant.

8.5 Phase Relationship between the Mass Flow Rate and the Temperature

Figures 10a and 10b present the variation of the Facet Averaged Temperature and mass flow rate at the exit of the regenerator and at the exit of the pulse tube, respectively, for a time period after the periodic state is attained. Radebaugh [7] has shown that the phase angle between mass flow rate and temperature to be very important in determining the performance of OPTR and other designs than the heat pumping even though heat pumping is the major mechanism in BPTR. The results obtained are for Model 4 with thermal non-equilibrium in the porous zones. It can be seen that at the exit of the regenerator, the temperature is leading the mass flow rate by a small phase angle. At the exit of the pulse tube, the mass flow rate and the temperature are almost out of phase. This condition is expected because the analysis is performed for no load condition, which means that the enthalpy flow through the pulse tube is small and is mainly due to the loss in the regenerator and the heat conduction in the pulse tube wall.

9. Conclusions

A sophisticated approach, taking into account the complete set of axi-symmetric flow conservation equations and finite wall thickness, is adopted for modeling an inertance type pulse tube refrigerator for thermal equilibrium and thermal non-equilibrium conditions of porous zones. The results obtained from the present model are expected to be more realistic compared to the simplified analyses like phasor and linear network, reported in literature. The effect of axial conduction on the performance of pulse tube is analyzed by introducing finite wall thickness for the components. This facilitates the quantification of the amount of axial heat conduction and the heat transfer between pulse tube wall and the gas. The cold heat exchanger temperature is higher with wall thickness taken into account. Thus the effect of axial heat conduction reduces the performance of pulse tube system. The dynamic characteristics of the pulse tube are analyzed with the help of a time constant for pulse tube wall and other porous zones. The cold end temperature has an inverse relation with time constant of the pulse tube wall whereas the cooldown time has direct relation with time constant due to higher heat storage. The decrease in cold end temperature with increase in pulse tube length is mainly due to the reduction of axial heat conduction and also due to the considerable reduction of heat transfer coefficient between pulse tube gas. It is has been shown that more heat pumping between gas and pulse tube wall increases the cold heat exchanger temperature. The oscillatory flow solid-fluid interactions are modeled with the more realistic thermal non-equilibrium model for porous zones. Thermal non-equilibrium in the porous zones results in higher temperatures in the cold heat exchanger. It is found that the contribution due to Forchheimer term is quite significant in the analysis of flow through porous medium. The compressor work increases with increase in length of pulse tube. It can be concluded that for the 4 mm diameter pulse tube, length-to-diameter ratios ranging from 10 to 20 are beneficial. Pulse tube refrigerator modeling with CFD packages is helpful for thermal design except for the problem of large computing times.

Acknowledgments

The authors gratefully acknowledge the help of the staff of the Super-computing Education and Research Centre (SERC) of the Indian Institute of Science, Bangalore, for running our FLUENT model. The authors express their sincere thanks to Prof. P.V. Desai, Prof. S.M. Ghiaasiaan and Dr. J.S. Cha of the Georgia Institute of Technology for many helpful suggestions and communications.

References

[1] W.E. Gifford, G.H. Kyanka, Reversible pulse tube refrigeration, Advances in Cryogenics Engineering 12 (1964) 619-630.

[2] P.C.T. de Boer, Thermodynamic analysis of the basic pulse-tube refrigerator, Cryogenics 34 (1994) 699-711.

[3] E.I. Mikulin, A.A. Tarasov, M.P. Shkrebyonock, Low temperature expansion tubes, Advances in Cryogenics Engineering 29 (1984) 629-637.

[4] S. Zhu, W. Peiyi, C. Zhongqi, Double inlet pulse tube refrigerator: An important improvement, Cryogenics 30 (1990) 514-520.

[5] P.R. Roach, A. Kashani, Pulse tube coolers with an inertance tube: Theory, modeling and practice, Advances in Cryogenic Engineering 43 (1998) 1895-1902.

[6] Rea, S.N. A study of thermal regenerators subjected to rapid pressure and flow cycling PhD Thesis, MIT, USA (1966).

[7] Radebaugh, R. A review of pulse tube refrigeration, Advances in Cryogenic Engineering 35 (1988) 1191-1205

[8] A. Razani, C. Dodson, B. Flake, T. Roberts, The effect of phase-shifting mechanism on energy and exergy flow in pulse tube refrigerators, Advances in Cryogenic Engineering 51-B (2005) 1572-1597.

[9] B.J. Huang, M.D. Chuang, System design of orifice pulse tube refrigerator using linear flow network analysis, Cryogenics 36 (11) (1996) 889-902.

[10] S. Zhu, Y. Matsubara, Numerical method of Inertance tube pulse tube refrigerator, Cryogenics 44 (2004) 649-660.

[11] J P. Harvey, Oscillatory Compressible Flow and Heat Transfer in Porous Media-Application to Cryocooler Regenerators, Ph.D. Thesis, Georgia Institute of Technology, Atlanta, Ga, 2003.

[12] J.S. Cha, S.M. Ghiaasiaan, P.V. Desai, J.P. Harvey, C.S. Kirkconnell, Multi-dimensional flow effects in pulse tube refrigerators, Cryogenics 46 (2006) 658–665.

[13] F. Barrett, R. Arsalan, Modeling pulse tube cryocoolers with CFD, Advances in Cryogenic Engineering 49 (2004) 1493–1499.

[14] B. Flakes, A. Razani, Modeling pulse tube cryocoolers with CFD, Proceedings of the international cryogenics engineering conference, 2003 1493–1499.

[15] M. Tanaka., I. Yamashita, F. Chisaka, Flow and heat transfer characteristics of Stirling engine regenerator in an oscillating flow, JSME International Journal 33 (II) (1990) 283-289.

[16] J.C.Y. Koh, Fortini Anthony, Prediction of thermal conductivity and electrical resistivity of porous metallic materials, International Journal of Heat Mass Transfer 16 (1973) 2013–2022.
[17] C. Li, G.P. Peterson, The effective thermal conductivity of wire screen, International Journal of Heat and Mass Transfer 49 (2006) 4095–4105.
[18] T.R. Ashwin, G.S.V.L. Narasimham and S. Jacob, Comparative numerical study of pulse tube refrigerators, Cryocoolers 15 (2009) 271-280.
[19] T.R Ashwin, G.S.V.L Narasimham, Subhash Jacob, Numerical modeling of inertance tube pulse tube refrigerator, Proceedings of CHT-08, ICHMT International Symposium on Advances in Computational Heat Transfer, Volume 1, 2008.
[20] Fluent 6.3 User's Guide, Fluent .Inc, http://www.fluentusers.com/

Figure Captions

Fig.1a. Integrated model of inertance tube pulse tube refrigerator (1) Compressor, (2) Transfer Line (3) After cooler (4) Regenerator (5) Cold heat exchanger (6) Pulse Tube (7) Hot heat exchanger (8) Inertance Tube (9) Buffer (10) Wall.
(b) Schematic of inertance tube pulse tube refrigerator with finite wall thickness.

Fig.2. Comparison of the present cooldown characteristics with that of Cha et al. [12].

Fig.3. Facet Average (FA) Temperature and Pressure at the exit of cold heat exchanger. **(a)** After 5 milliseconds from starting. **(b).** After 432.268 seconds from starting.

Fig.4a. Instantaneous pressure variation in the regenerator. **(b)** Axial temperature variation for the full pulse tube system after 432.668 seconds. **(c)** Velocity vector plots at the junction of transfer line and compressor cooler.

Fig.5a. VAMS Temperature Vs Cooldown time for different models with wall and with thermal- equilibrium of porous zone. **(b).** Variation of compressor input power with length-to-diameter ratio of the pulse tube

Fig.6. FAMS Temperature Vs Cooldown time of Model 3 with thermal- equilibrium of porous zones.

Fig.7a. VAMS Temperature and Heat Transfer Coefficient Vs Time Constant of Pulse tube Wall **(b)** Variation of pulse tube wall temperature, gas temperature and heat transfer coefficient over one cycle during cooldown. **(c)** Average axial heat conduction and Average Pulse tube Gas- Solid heat transfer Over one cycle w.r.t Figure 8b

Fig.8a. Cooldown characteristics of Model 4 with finite wall thickness **(b)** Axial temperature distribution inside regenerator **(c)** Axial temperature distribution inside hot heat exchanger

Fig.9a. Plot of velocity, Darcy term and Forcheimmer at particular nodal point inside the regenerator **(b)** Cold heat exchanger.

Fig.10a. Variation of Facet Average (FA) temperature and mass flow rate at the exit of the regenerator. **(b)** At the beginning of the hot heat exchanger.

List of Tables

Table 1. Geometry details and Boundary Conditions of Model 1

Components and	Diameter(mm)	Length(mm)	Wall	Wall	Boundary

Part Number			thickness(mm)	Material	condition
Compressor Piston (1)	15	6 (stroke length)	----	-----	Adiabatic
Transfer Line (2)	2	100	0.3	SS-304	Adiabatic
Compressor cooler (Whx1)(3)	6	16	0.3	OFHC-Cu	300K
Regenerator (4)	6	60	0.3	SS-304	Adiabatic
Cold heat exchanger (Chx) (5)	4	4	1	OFHC-Cu	Adiabatic
Pulse tube (6)	4	30 (variable)	0.3	Titanium	Adiabatic
Hot heat exchanger(Whx2) (7)	4	15	0.3	OFHC-Cu	300K
Inertance tube (8)	0.6	300	0.3	SS-304	Adiabatic
Buffer (9)	30	80	0.3	SS-304	Adiabatic

Table 2. Length to Diameter ratios of pulse tubes

	Pulse Tube Diameter	Pulse Tube Length (mm)	L/D Ratio

	(mm)		
Model 1	4	30	7.5
Model 2	4	50	12.5
Model 3	4	75	18.75
Model 4	4	100	25
Model 5	4	150	37.5

Table :3 : Results for various models of pulse tube refrigerators

Length of	Area average	Time constant	Mass Ratio	VAMS	Cool down

Pulse tube (mm)	h between gas and pulse tube wall ($W/m^2 K$)	for pulse tube Wall ψ_{pt} (s)	M_{pt} / M_{reg}	Temperature at exit of CHX	time in seconds (t_{90})
30	6367	0.1337	0.062701	163.8	25
50	4393	0.17759	0.104502	152.4	27
75	2931	0.2904	0.156752	140.0	46
100	1024	0.8315	0.209003	132.2	209
150	413	2.0611	0.313505	113.1	306

Table :4 : Time constant for various porous zones

Name of Porous Zones	Average heat transfer coefficient by Tanaka [15]	Time Constant (ψ)

	$(W/m^2 K)$	
Whx1	13865	0.01004
Regenerator	15752	0.009556
Chx	34365	0.004051
Whx2	24540	0.005673

Figures

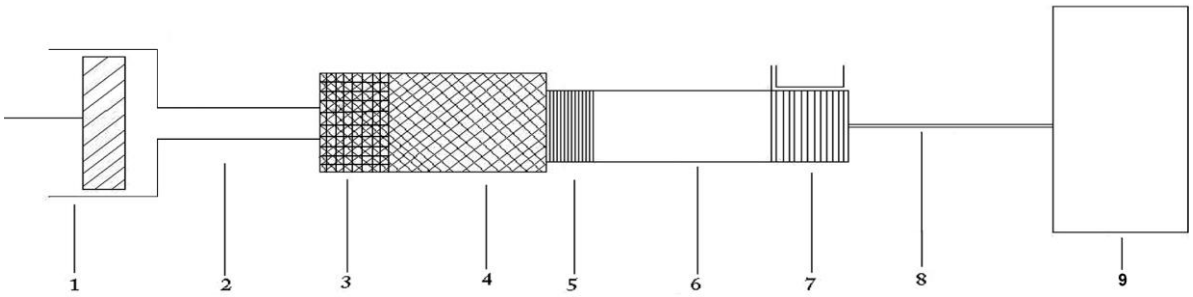

Fig.1a

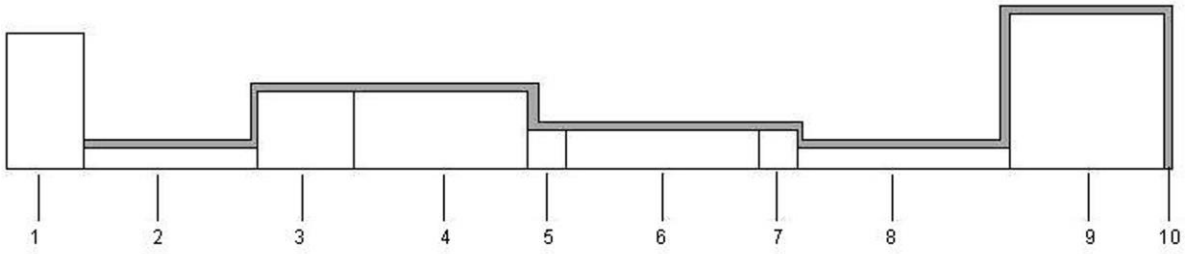

Fig.1b

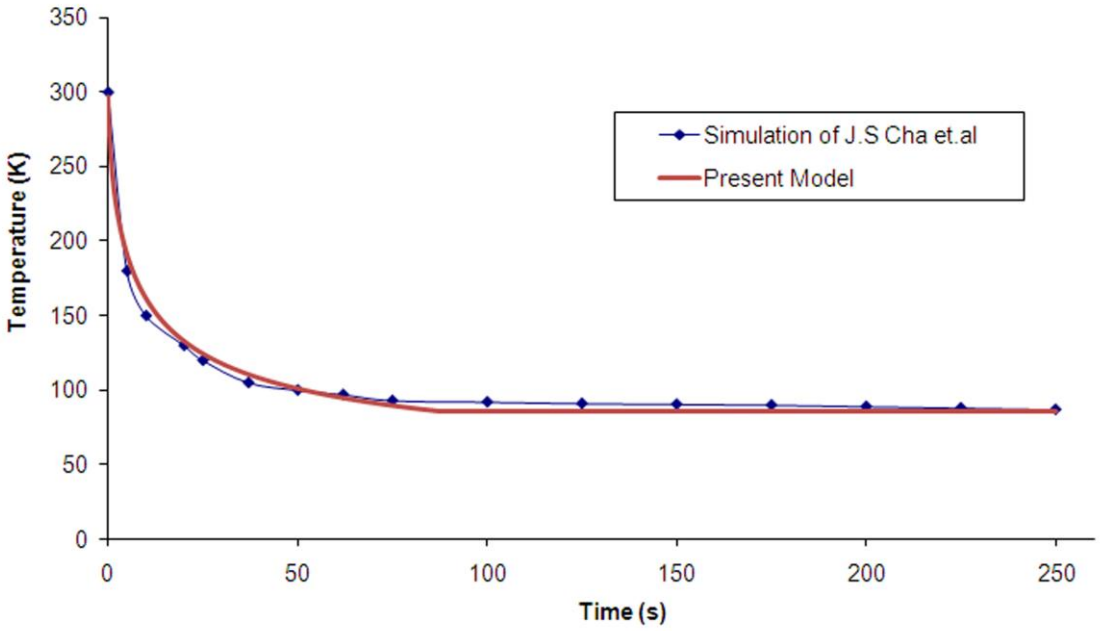
350
300
250
200
150
100
50
0
Temperature (K)
0
50
100
150
200
250
Time (s)
Simulation of J.S Cha et.al
Present Model

Fig.2

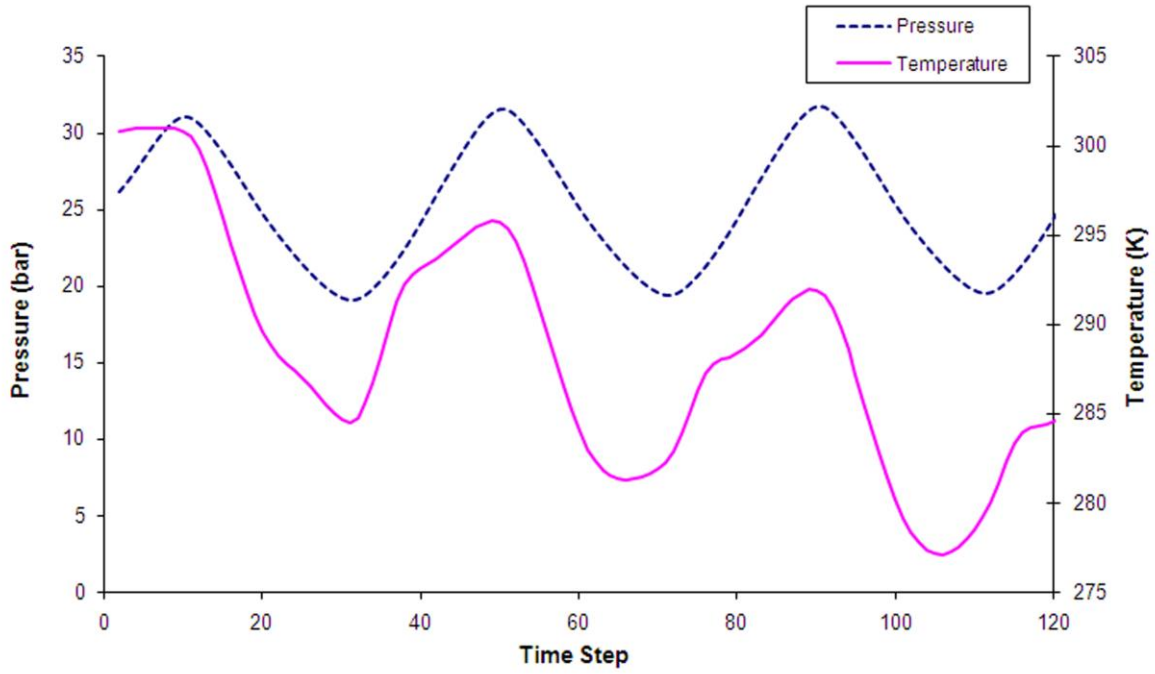
Pressure
Temperature
Pressure (bar)
Temperature (K)
Time Step
0
5
10
15
20
25
30
35
275
280
285
290
295
300
305
0
20
40
60
80
100
120

Fig 3a

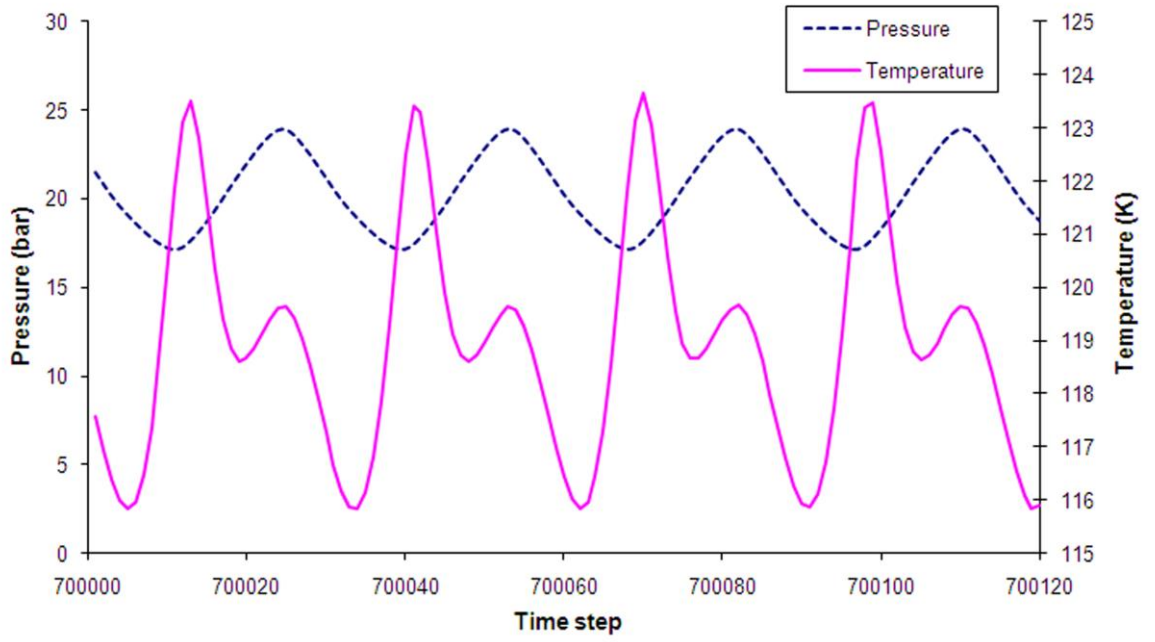
Pressure
Temperature
Pressure (bar)
Temperature (K)
Time step
0
5
10
15
20
25
30
115
116
117
118
119
120
121
122
123
124
125
700000
700020
700040
700060
700080
700100
700120

Fig 3b

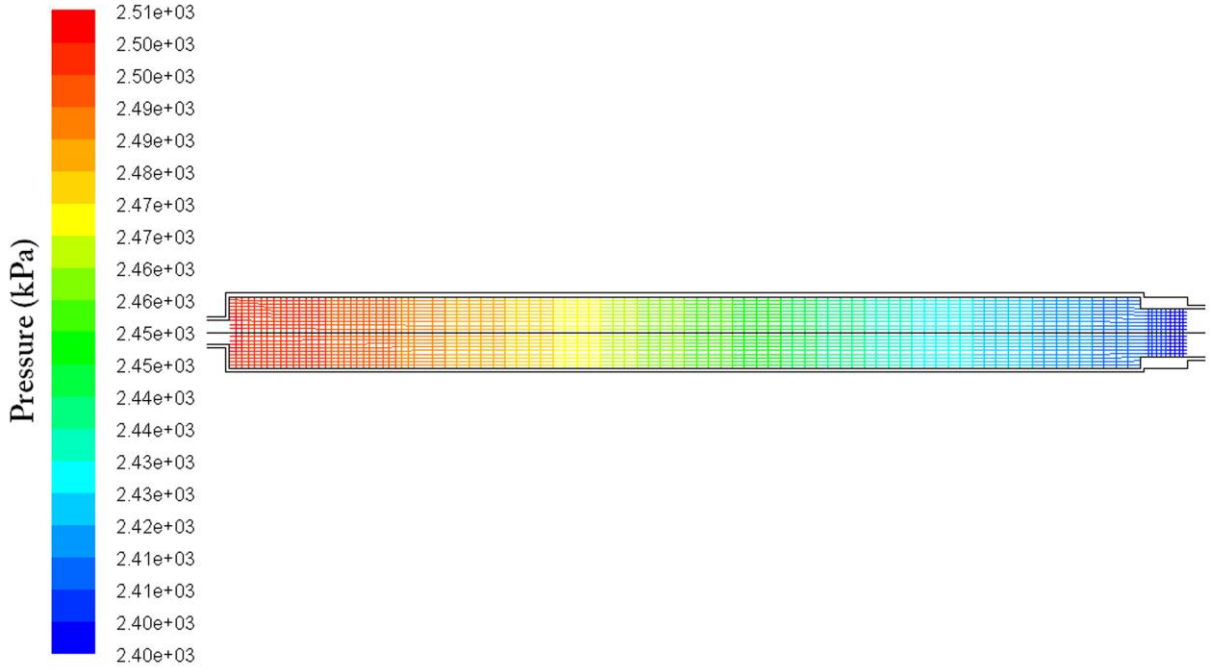
Pressure (kPa)
2.51e+03
2.50e+03
2.50e+03
2.49e+03
2.49e+03
2.48e+03
2.47e+03
2.47e+03
2.46e+03
2.46e+03
2.45e+03
2.45e+03
2.44e+03
2.44e+03
2.43e+03
2.43e+03
2.42e+03
2.41e+03
2.41e+03
2.40e+03
2.40e+03

Fig 4a

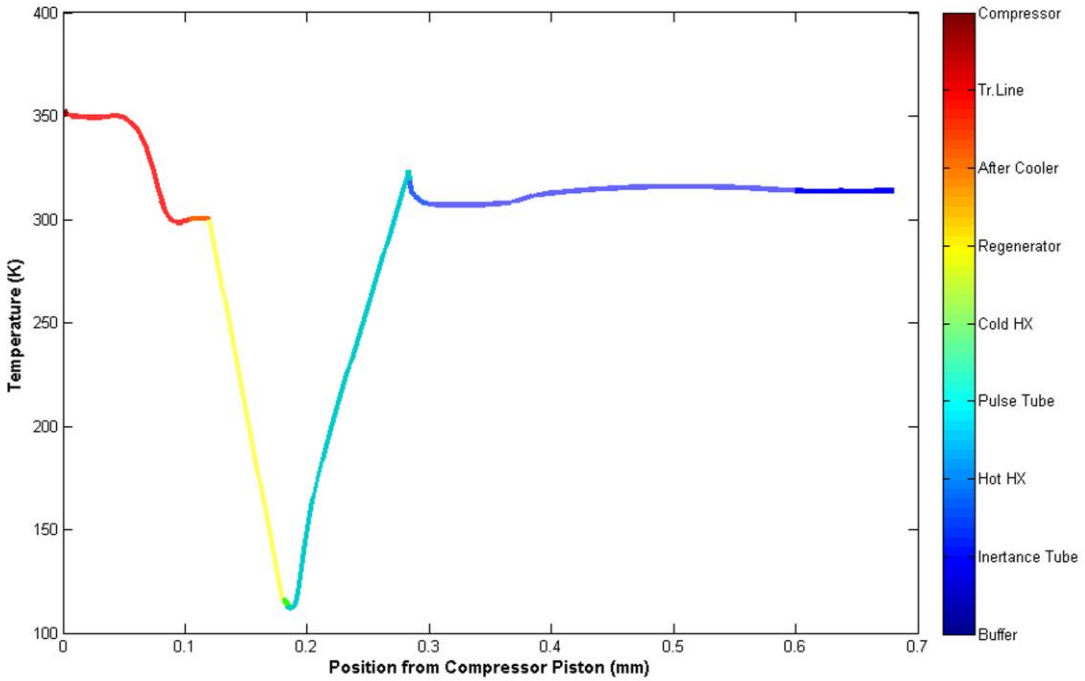
Temperature (K)
400
350
300
250
200
150
100
0
0.1
0.2
0.3
0.4
0.5
0.6
0.7
Position from Compressor Piston (mm)
Compressor
Tr.Line
After Cooler
Regenerator
Cold HX
Pulse Tube
Hot HX
Inertance Tube
Buffer

Fig 4b

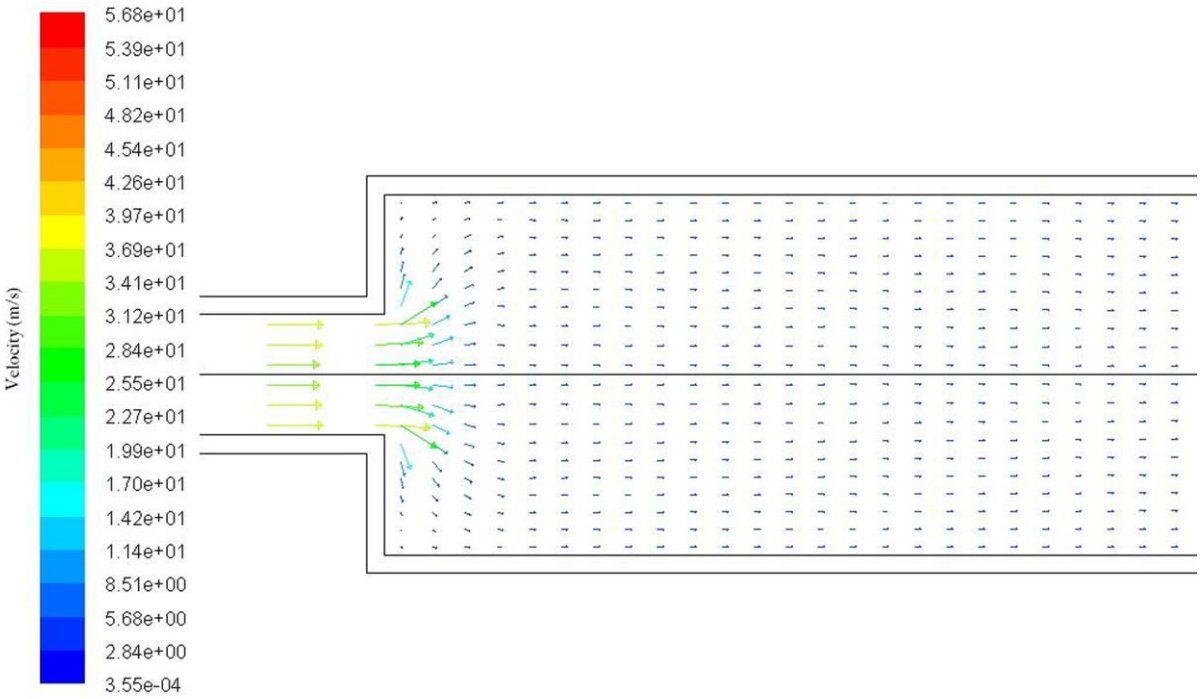
Velocity (m/s)
5.68e+01
5.39e+01
5.11e+01
4.82e+01
4.54e+01
4.26e+01
3.97e+01
3.69e+01
3.41e+01
3.12e+01
2.84e+01
2.55e+01
2.27e+01
1.99e+01
1.70e+01
1.42e+01
1.14e+01
8.51e+00
5.68e+00
2.84e+00
3.55e-04

Fig 4c

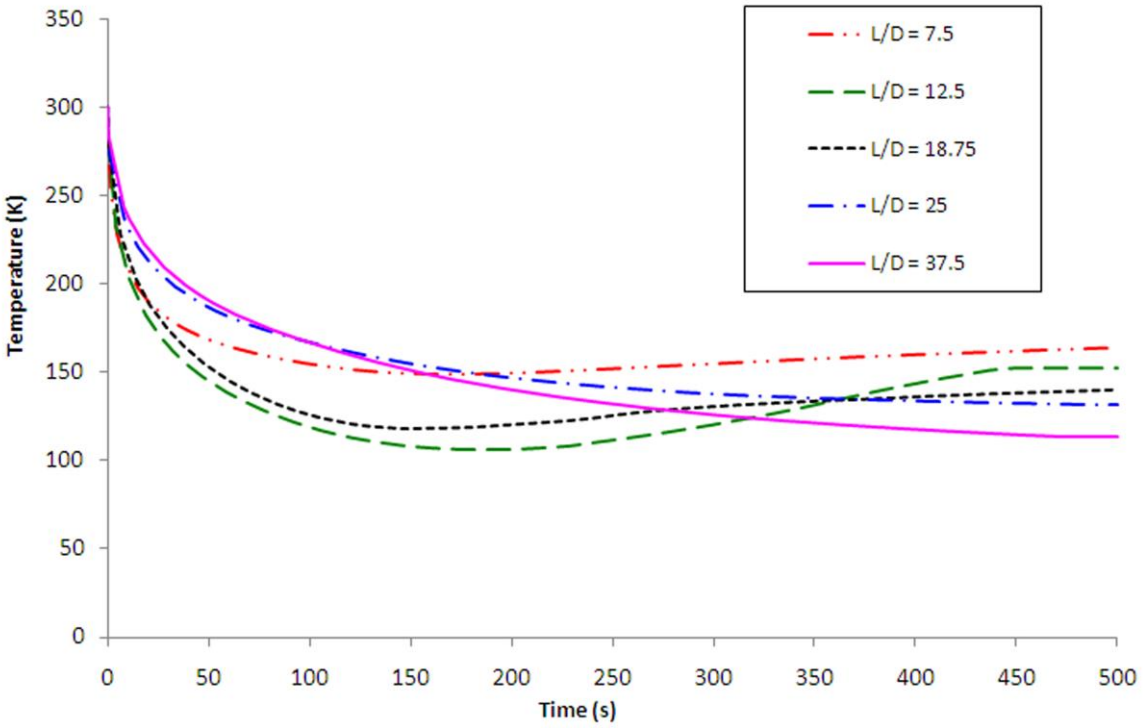
L/D = 7.5
L/D = 12.5
L/D = 18.75
L/D = 25
L/D = 37.5
Temperature (K)
Time (s)
0
50
100
150
200
250
300
350
400
450
500

Fig 5a

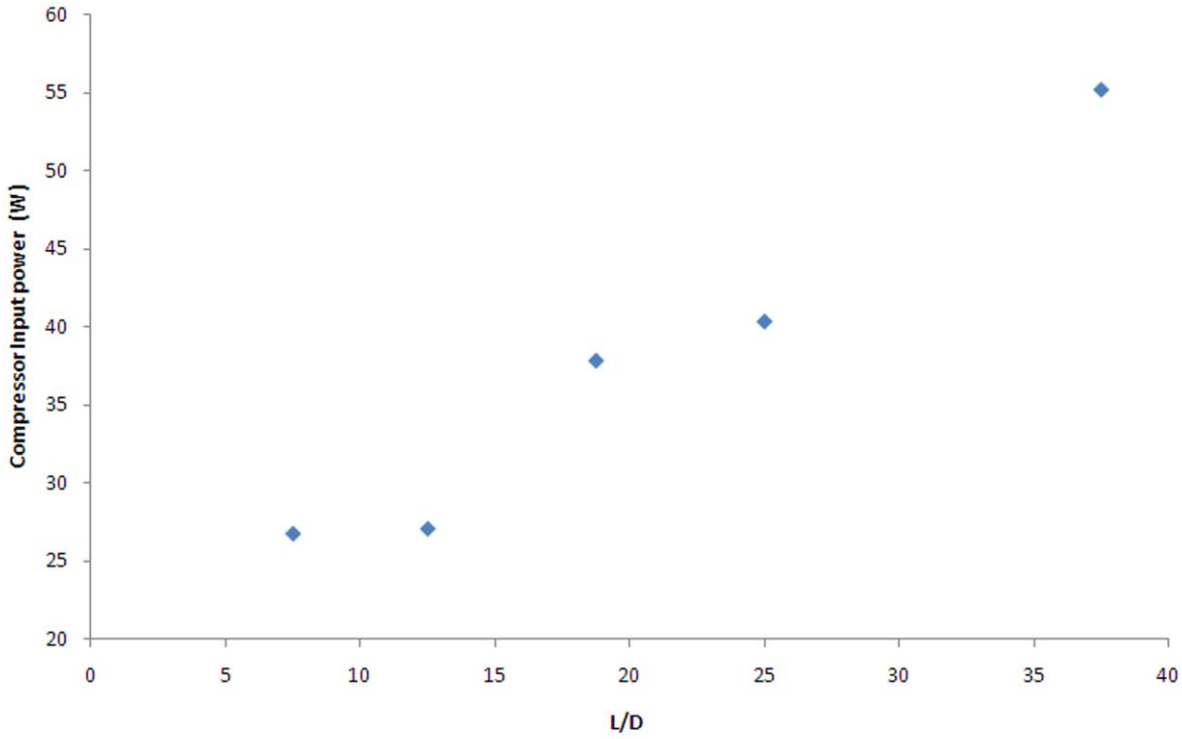
Compressor Input power (W)
L/D
20
25
30
35
40
45
50
55
60
0
5
10
15
20
25
30
35
40

Fig 5b

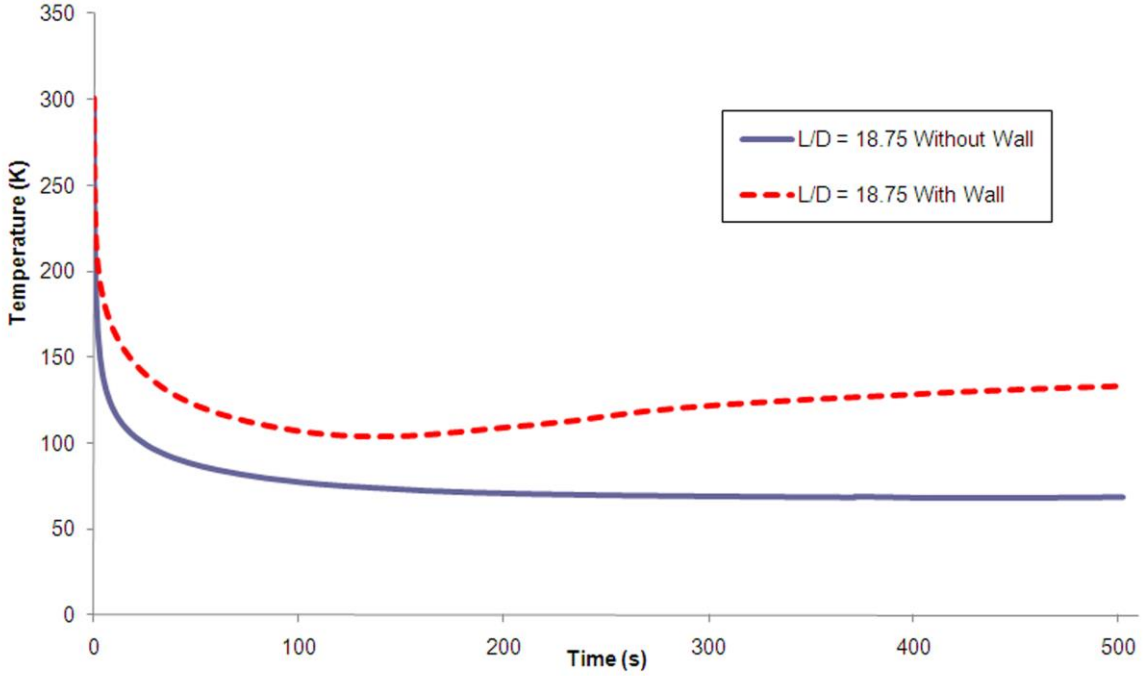
350
300
250
200
150
100
50
0
Temperature (K)
0
100
200
300
400
500
Time (s)
L/D = 18.75 Without Wall
L/D = 18.75 With Wall

Fig 6

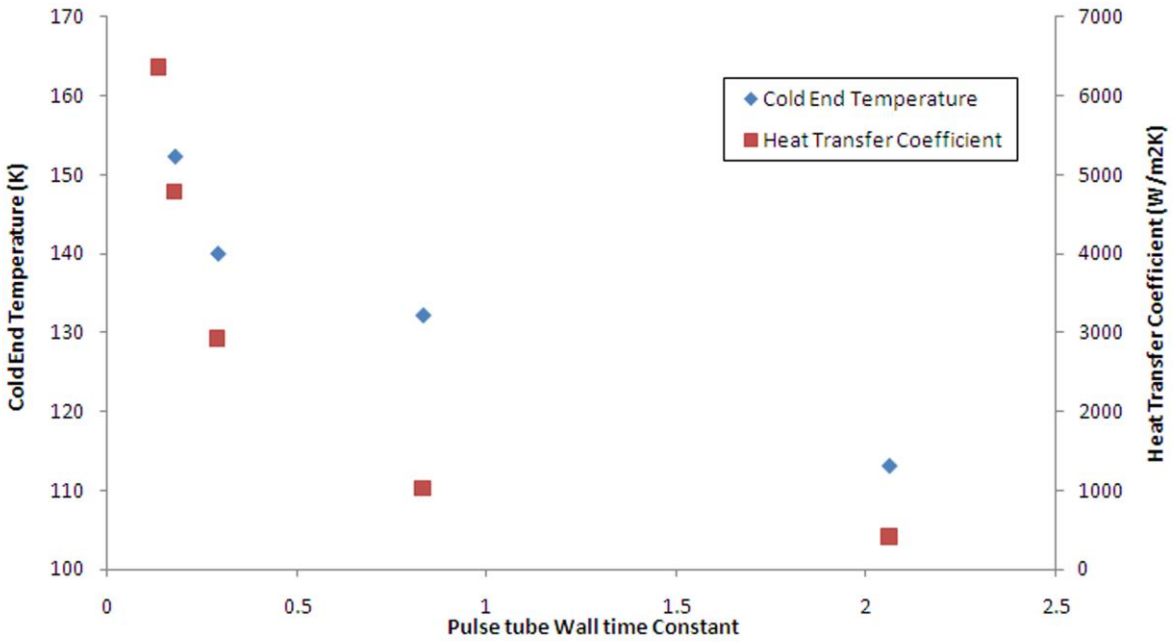
Cold End Temperature
Heat Transfer Coefficient
Cold End Temperature (K)
Heat Transfer Coefficient (W/m2K)
Pulse tube Wall time Constant
170
160
150
140
130
120
110
100
7000
6000
5000
4000
3000
2000
1000
0
0
0.5
1
1.5
2
2.5

Fig 7a

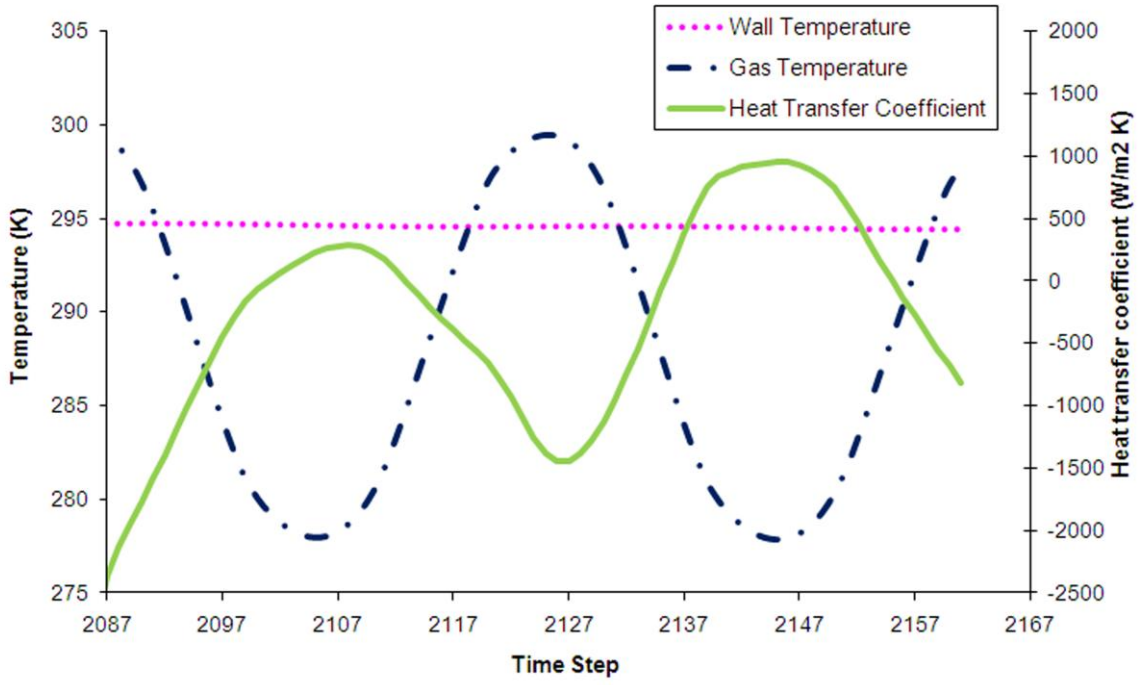
Wall Temperature
Gas Temperature
Heat Transfer Coefficient
Temperature (K)
Heat transfer coefficient (W/m2 K)
Time Step
305
300
295
290
285
280
275
2000
1500
1000
500
0
-500
-1000
-1500
-2000
-2500
2087
2097
2107
2117
2127
2137
2147
2157
2167

Fig 7b

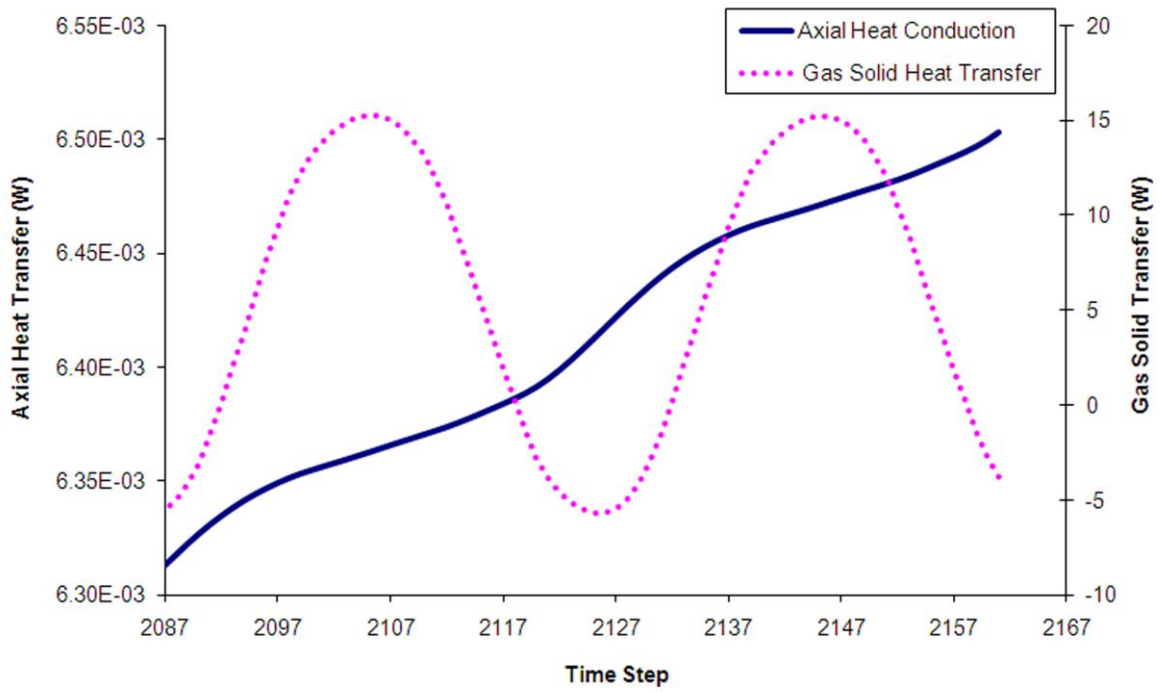
Axial Heat Conduction
Gas Solid Heat Transfer
6.55E-03
6.50E-03
6.45E-03
6.40E-03
6.35E-03
6.30E-03
Axial Heat Transfer (W)
20
15
10
5
0
-5
-10
Gas Solid Transfer (W)
2087
2097
2107
2117
2127
2137
2147
2157
2167
Time Step

Fig 7c

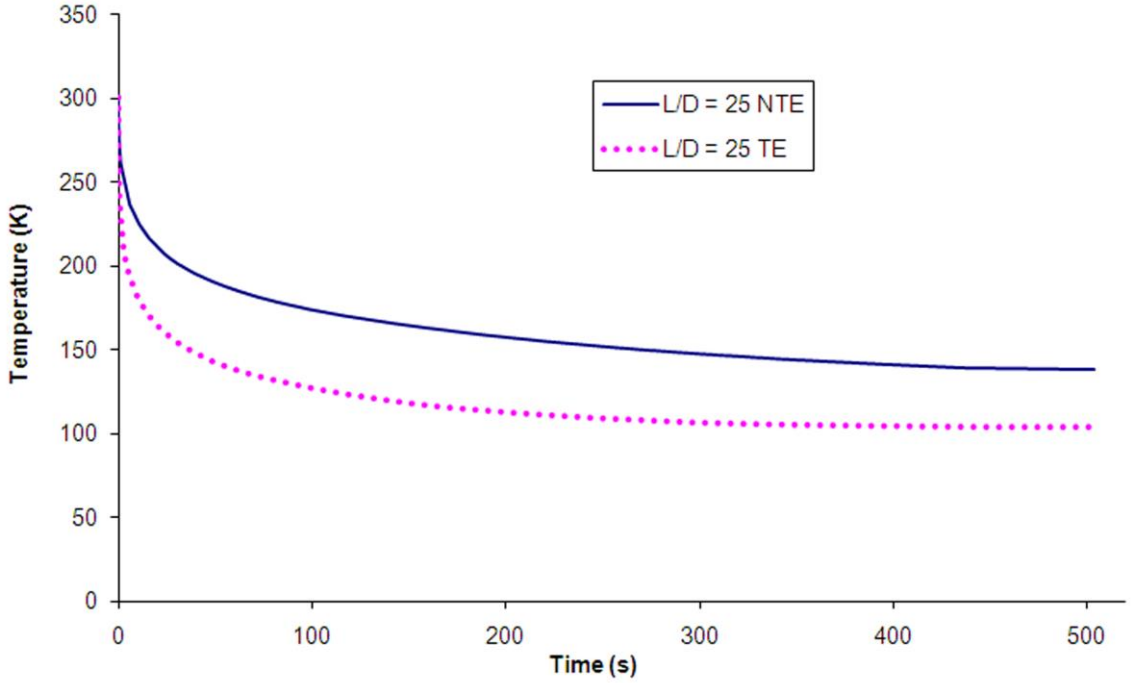
350
300
250
200
150
100
50
0
Temperature (K)
0
100
200
300
400
500
Time (s)
L/D = 25 NTE
L/D = 25 TE

Fig 8a

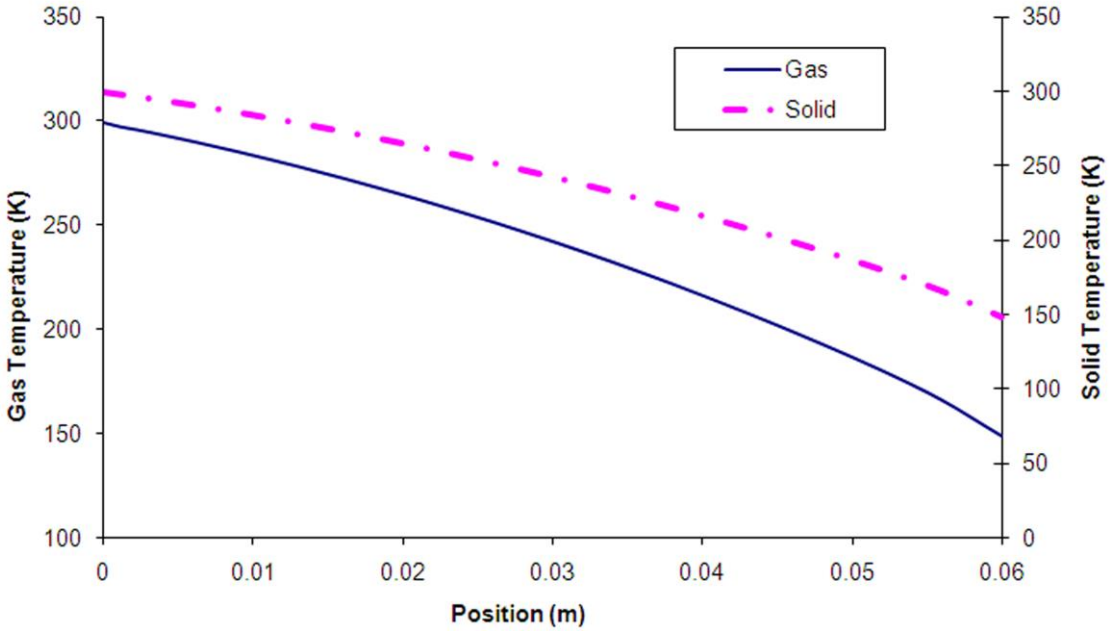
350
300
250
200
150
100
Gas Temperature (K)
0
0.01
0.02
0.03
0.04
0.05
0.06
Position (m)
350
300
250
200
150
100
50
0
Solid Temperature (K)
Gas
Solid

Fig 8b

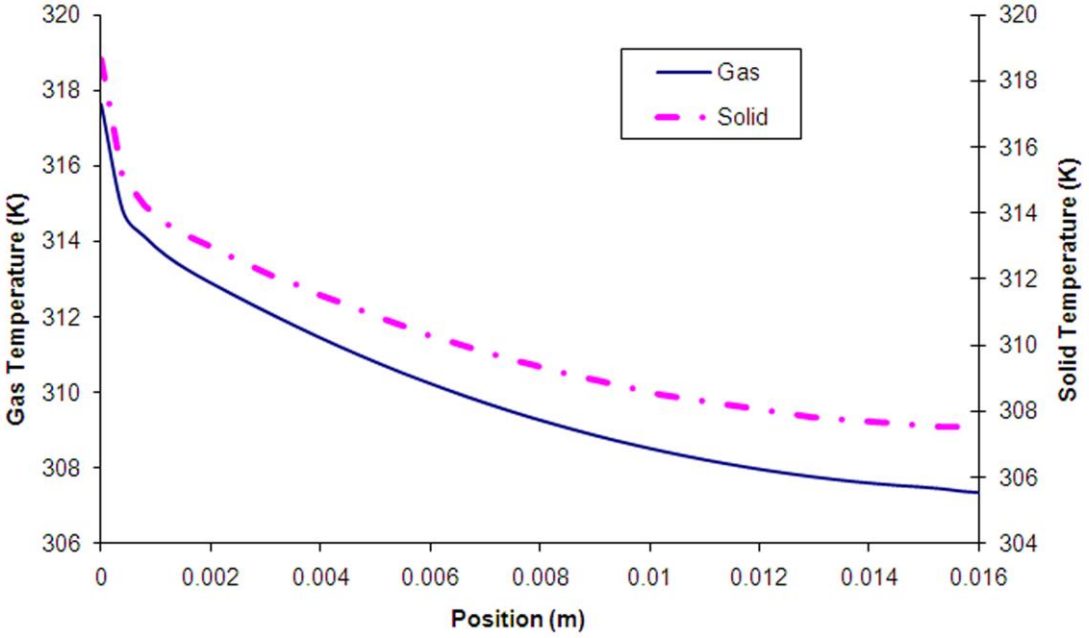
Gas
Solid
Gas Temperature (K)
Solid Temperature (K)
Position (m)
320
318
316
314
312
310
308
306
304
0
0.002
0.004
0.006
0.008
0.01
0.012
0.014
0.016

Fig 8c

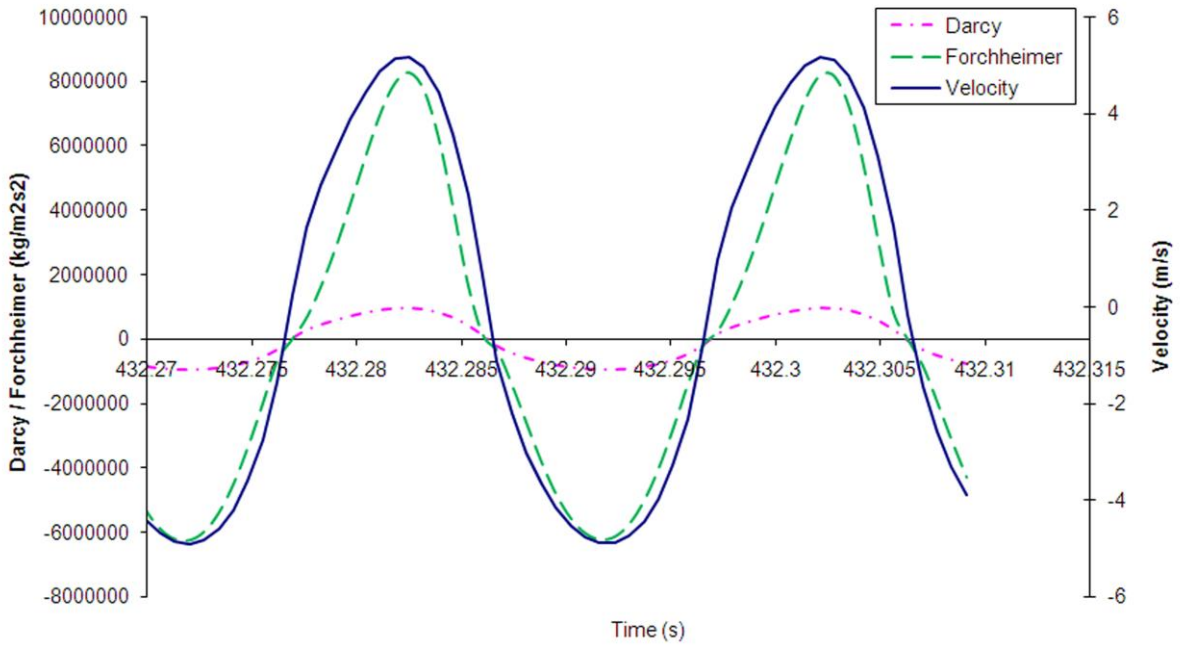
Darcy
Forchheimer
Velocity
10000000
8000000
6000000
4000000
2000000
0
-2000000
-4000000
-6000000
-8000000
6
4
2
0
-2
-4
-6
432.27
432.275
432.28
432.285
432.29
432.295
432.3
432.305
432.31
432.315
Darcy / Forchheimer (kg/m2s2)
Velocity (m/s)
Time (s)

Fig 9a

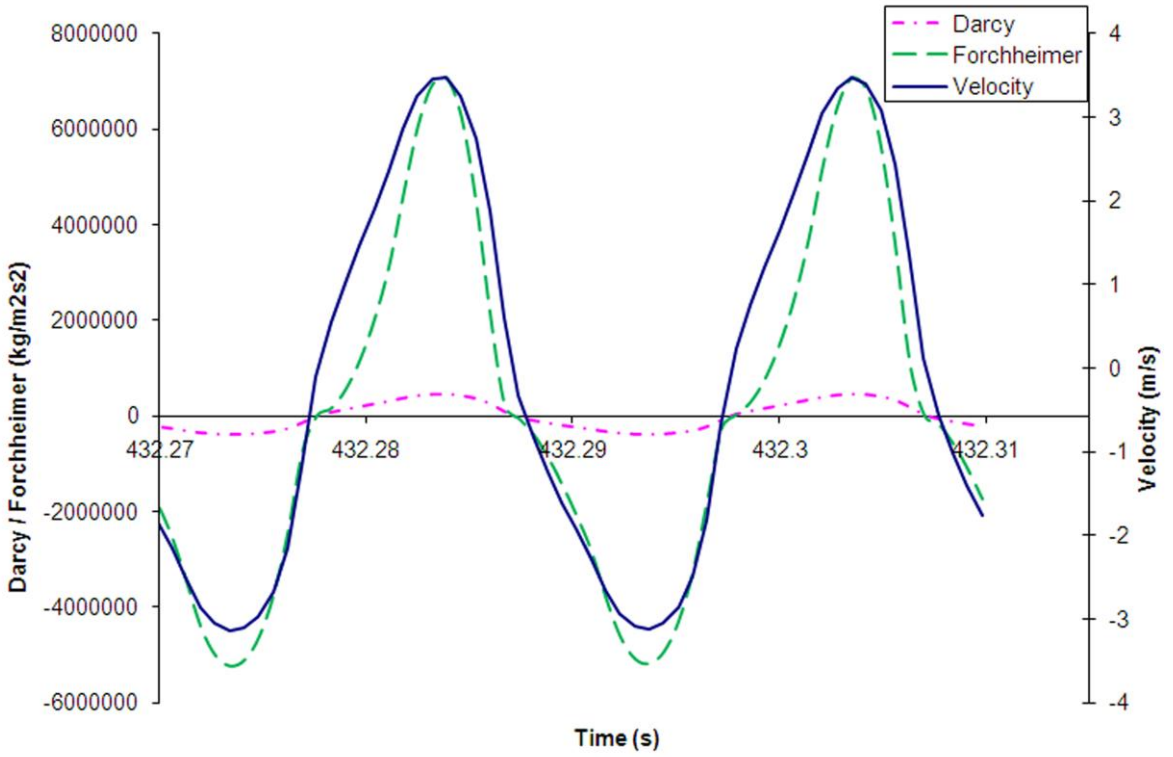
Darcy
Forchheimer
Velocity
8000000
6000000
4000000
2000000
0
-2000000
-4000000
-6000000
4
3
2
1
0
-1
-2
-3
-4
432.27
432.28
432.29
432.3
432.31
Darcy / Forchheimer (kg/m2s2)
Velocity (m/s)
Time (s)

Fig 9b

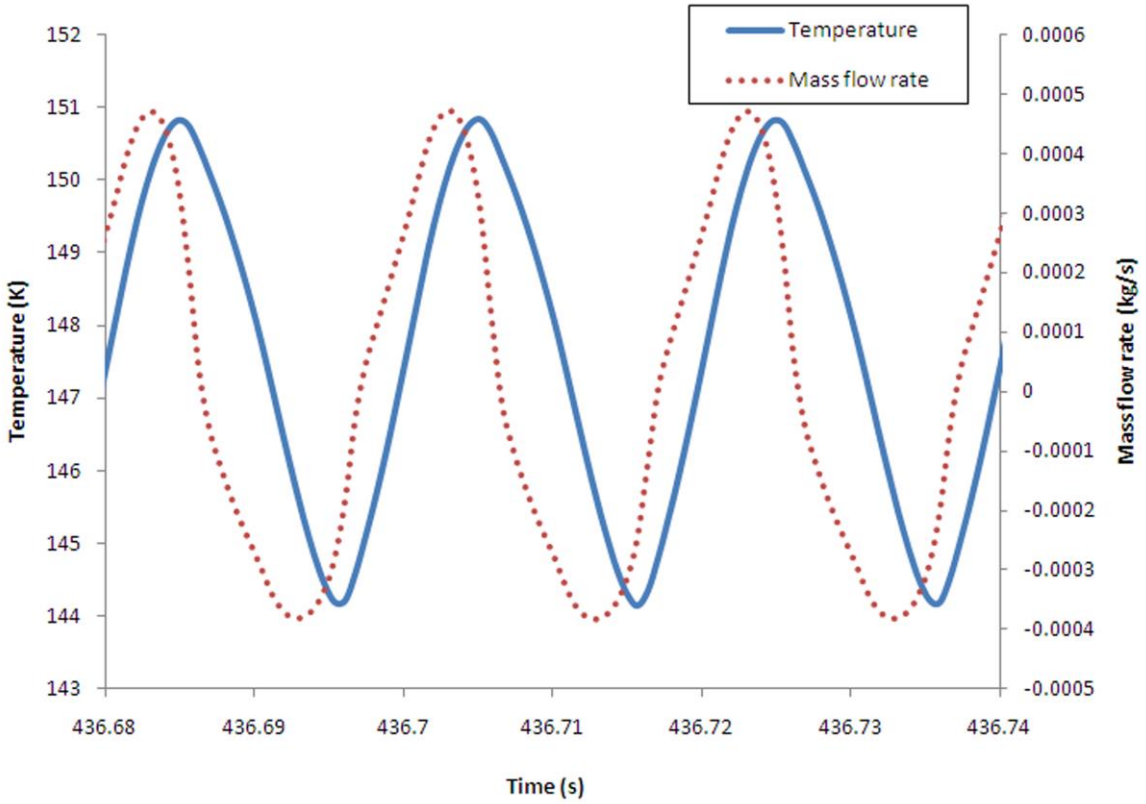

Fig 10a

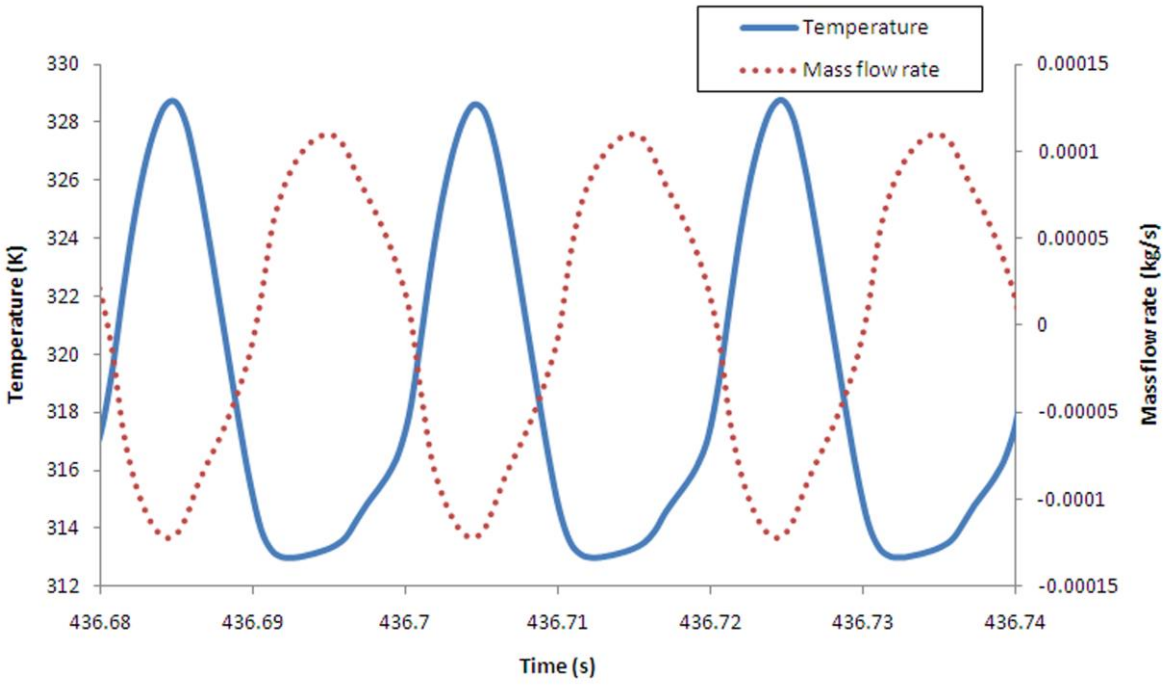

Fig 10b